
EFFECTS OF SALT AND ASH ON THE HIGH-TEMPERATURE CORROSION BEHAVIOUR OF Ni-25Cr ALLOY IN WET CO₂ GAS AT 650°C

Yuchen Cai, Jianqiang Zhang*, David J. Young

School of Materials Science and Engineering, University of New South Wales, Sydney, NSW 2052, Australia

*Corresponding author: j.q.zhang@unsw.edu.au

ABSTRACT

A model Ni-25Cr (wt.%) alloy coated with chloride salts, industrial coal ash, and mixtures of these salts with coal ash (ash/salt weight ratios: 90/10, 50/50, 25/75) was exposed in Ar-60CO₂-20H₂O at 650°C for 100 h and 300 h. For comparison, the alloy without any deposit was also exposed to the same gas.

The alloy without any deposit developed a uniform internal oxidation zone (IOZ) containing Cr-rich oxide, below an external layer and metallic nickel nodules surmounted by a thin NiO scale.

Ni-25Cr covered by 100% ash behaved quite similarly to the one in the gas-only case, despite the disappearance of extruded metallic Ni layer and the thicker IOZ layer (gas-only: 6 μm, ash-only: 9 μm).

After starting to add chloride salt to the deposit, a localised structure formed. Localised thick Cr₂O₃ scale containing encapsulated Ni metal with underlying subsurface alloy porosity were found. This localised structure occupied 10% of the whole surface in the 10% salt + 90% ash case, while the rest 90% remained the same as in the gas-only case. As the salt amount increased to 50%, the structure with subsurface voids occupied 80% of the whole surface, while a duplex layer formed on the remaining 20% of the sample surface.

Two different structures are also found in the 100% salt case. Predominantly, a multilayered scale of NiO over a thin Cr₂O₃ layer formed, with an underlying IOZ containing Cr-rich oxide precipitates. Local regions of thick Cr₂O₃ scale containing encapsulated Ni metal with underlying subsurface alloy porosity were found.

Keywords: High-temperature corrosion, chlorides, coal ash, Ni-based alloy

INTRODUCTION

Oxyfuel combustion has been developed as one of the leading technologies considered for capturing CO₂ from power plants with CCS [1]. Instead of using air to burn the coal, this approach uses only pure oxygen. Part of the flue gas is recycled back into the furnace or oiler in order to regulate the flame temperature. The flue gas mainly consists of CO₂ and H₂O, allowing easier CO₂ capture and subsequent sequestration [2].

However, this flue gas is very corrosive at high temperatures. Traditional Fe-based alloys that withstand heat cannot endure. In this case, Ni-based alloys are considered due to their better high temperature mechanical capabilities and corrosion resistance. Besides the corrosive gas, solid species like chlorides and ashes contained in the flue gas can deposit on alloy surfaces, hence accelerating the corrosion process [3, 4]. Previous investigations [5, 6] have demonstrated that Ni-based alloys experience accelerated corrosion in the presence of chloride salts. The active oxidation brought on by chloride salts is the reason for the accelerated oxidation [6, 7]. However, the synergistic effects of salts and ash mixture need to be investigated.

This paper examines the corrosion behaviour of a Ni-25Cr model alloy, in wet CO₂ gas without and with deposits at 650°C. The effects of chloride salt, ash, and their mixtures are studied.

METHODS AND MATERIALS

A Ni-25Cr (wt. %) model alloy was prepared by arc melting pure metals Ni (99.95%), and Cr (99.995%), under a protective Ar-5%H₂ gas atmosphere, using a non-consumable tungsten electrode. The resulting alloy buttons were annealed for 50 h at 1100 °C under a flowing Ar-5%H₂ (vol. %) gas for homogenisation. Only a small deviation (± 0.3 wt. %) was found from the designed compositions of Ni-25Cr, confirmed by SEM-EDS analysis after homogenising.

The alloy was then cut into approximately 9 x 7 x 2 mm rectangles, and ground to a 1200-grit finish, followed by polishing to a 3- μ m finish and then electropolishing in 15% hydrochloric acid. The work-hardened surface zone that was introduced during sample preparation was removed using electropolishing. The Ni-25Cr grains were elongated, with sizes ranging from hundreds of microns to several millimetres.

For the gas-only experiment, the sample coupon was laid on a ceramic crucible with one face up to the gas atmosphere, for comparison with subsequent experiments with salt deposits. The ceramic crucible was placed in a horizontal alumina reactor sitting inside a tube furnace for isothermal oxidation at 650°C, and exposed to flowing gases for 300 h. The reaction gas composition was Ar-60%CO₂-20%H₂O (vol. %) with a linear flow rate of 2 cm/s. Argon and carbon dioxide inputs were controlled by mass-flow controllers. Wet gases were generated by passing the argon and carbon dioxide mixture through a water bath to first produce an excess amount of water vapour, which was then partially condensed inside a distillation column at a temperature set to achieve the required water vapour concentration [8]. The calculated equilibrium partial pressure of oxygen in the gas stream is 1.5×10^{-8} atm and carbon activity is 1.6×10^{-15} [9] (Table 1).

For salt-coated experiments, NaCl and KCl were dissolved in distilled water in a mass ratio of 1:1.25, corresponding to the lowest solidus temperature (657°C) [10]. Each solution was sprayed onto preheated sample surfaces to cause evaporation of the water. The coated samples were weighed after spraying, to ensure the deposit was within the 2.5 ± 0.5 mg/cm² range. The deposited samples were exposed in the same way as described above for the gas-only conditions. The chloride and sulphate salt experiments were carried out in different furnaces with the same settings to avoid contamination. Equilibrium gas pressures and carbon activity values, a_c , were calculated [10] for the cases with salts present, and the results are listed in Table 1.

Table 1. Equilibrium minority gas partial pressures (atm) and a_c at 650 °C, 1 atm

Species	Ar-60CO ₂ -20H ₂ O	Ar-60CO ₂ -20H ₂ O + NaCl + KCl
O ₂	1.5×10^{-8}	1.5×10^{-8}
HCl	-	5.8×10^{-6}
Cl ₂	-	1.2×10^{-14}
a_c	1.6×10^{-15}	1.6×10^{-15}
NaCl	-	6.9×10^{-6}
KCl	-	1.6×10^{-5}

For ash/ ash plus salt deposit experiments, the salt mixture was mixed with the Eraring ash (provided by industry, composition listed in Table 2) in a weight ratio of 1:9, 5:5, and 7.5:2.5. The resulting mixture was then put in ethanol to form a suspension. The suspension was applied to preheated specimens and dried on a hot pan. The coated samples were weighed to make sure salt + ash deposits were in the 30 ± 5 mg/cm² range. The resulting coated samples were exposed in the same way as described above for the salts-deposited specimens.

Table 2. Compositions of Eraring ash (wt. %)

Compositions	Eraring ash (wt. %)
SiO₂	64.6
Al₂O₃	24.4
Fe₂O₃	2.9
CaO	1.7
MgO	0.6
K₂O	2.3
Na₂O	0.7
LOI	2.8

*LOI stands for loss on ignition

All reacted samples were cold-mounted in epoxy resin for metallographic preparation. Cross-sections of deposited specimens were prepared using water-free lubricant to avoid the dissolution of any salts in the products. Reaction products in cross-sections were observed and analysed by using optical microscopy (OM), field emission scanning electron microscopy (FEI Nova NanoSEM 230 & 450) equipped with energy-dispersive X-ray spectroscopy (EDS; Bruker), and series focused ion beam (FIB) sectioning analysis performed on the FEI Helios G4 PFIB.

RESULTS

The optical micrograph shows the corrosion behaviour of Ni-25Cr under various deposits at 650°C in Fig. 1. For the gas-only case, the scale was composed of extruded metallic Ni with NiO on the top, along with uniformed Cr-rich IOZ. This structure was also observed in the 100% ash case, and was the dominant oxide structure in the 10% salt

(area percentage: 90%) and 100% salt (area percentage: 70%) cases. However, structure with very thick, porous external oxide with arrayed subsurface precipitates was dominant in the 50% and 75% salt cases.

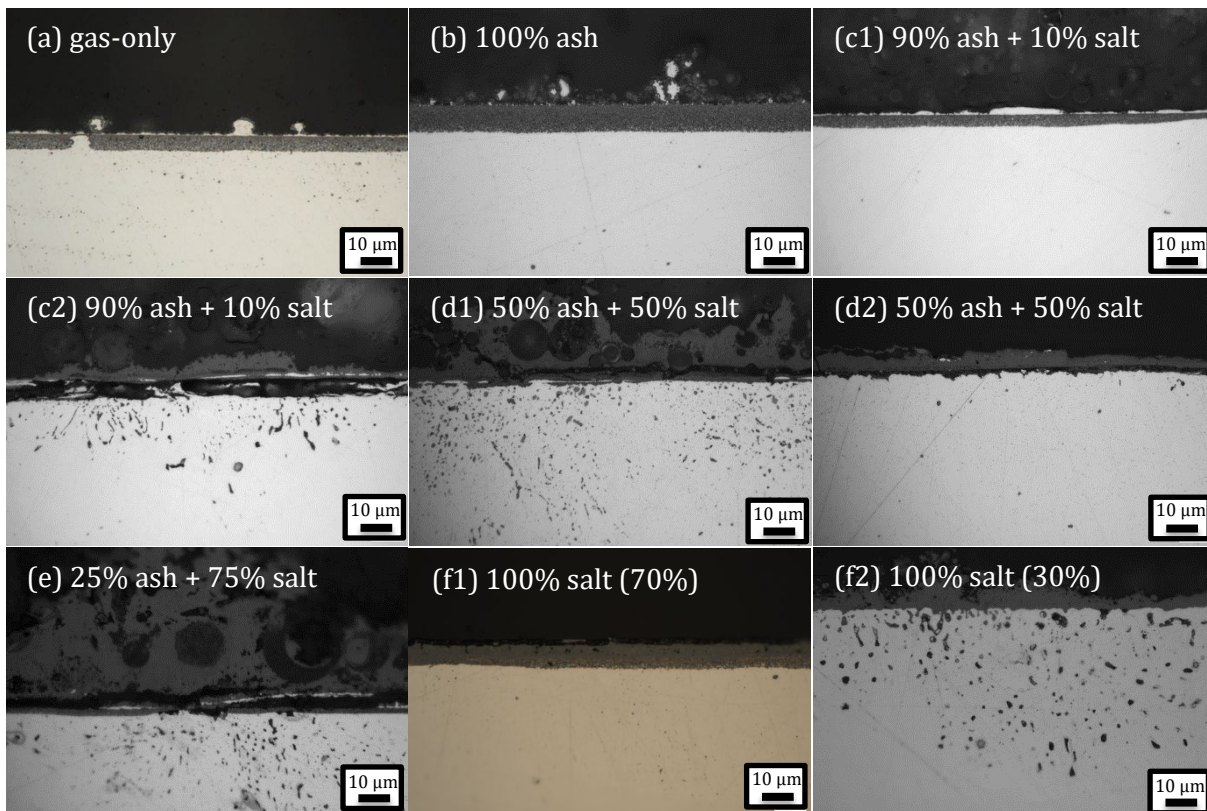


Figure. 1 – Cross-sectional optical micrographs of (a) gas-only, (b) 100% ash, (c) 90% ash + 10% salt, (d) 50% ash + 50% salt, (e) 25% ash + 75% salt, and (f) 100% salt covered Ni-25Cr after 300 h reactions at 650°C.

SEM-EDS mapping results for the gas-only case are shown in Fig. 2. The outer part of the reaction zone could be seen more clearly, to consist of a thin NiO layer surmounting a metallic nickel layer, according to the SEM-EDS mapping. The size and morphology of oxides in the internal oxidation zone varied with their location, very fine and densely distributed oxides near the surface, but relatively large rod-like precipitates at the reaction front (Fig. 2).

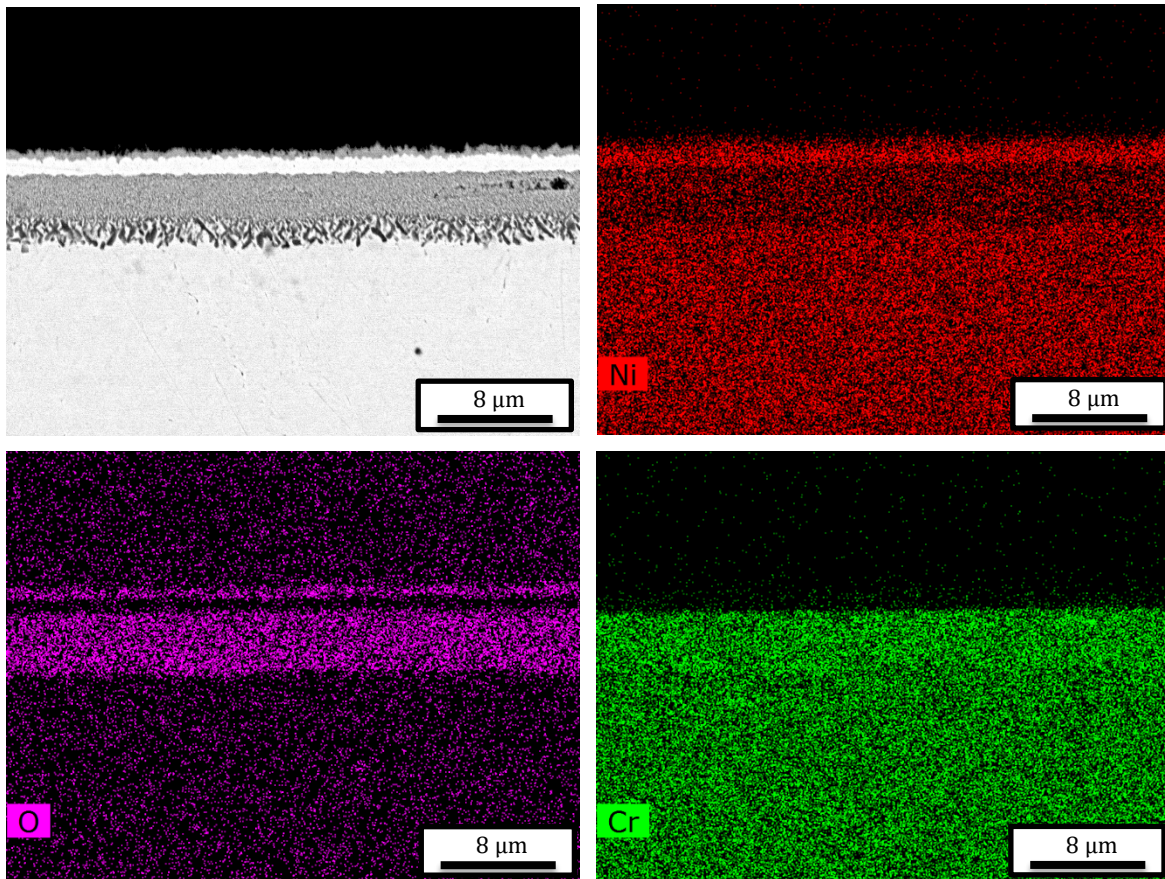


Figure. 2 – BSE-SEM cross-section and EDS mapping of Ni-25Cr after 300 h reaction in Ar-60CO₂-20H₂O at 650°C.

SEM-EDS mapping results for the 100% ash case are shown in Fig. 3, and it was found that fragmented NiO formed as the outermost layer, with uniform Cr-rich IOZ below it. Several ash particles could be detected above the scale, but no enrichment of chloride salt elements was found.

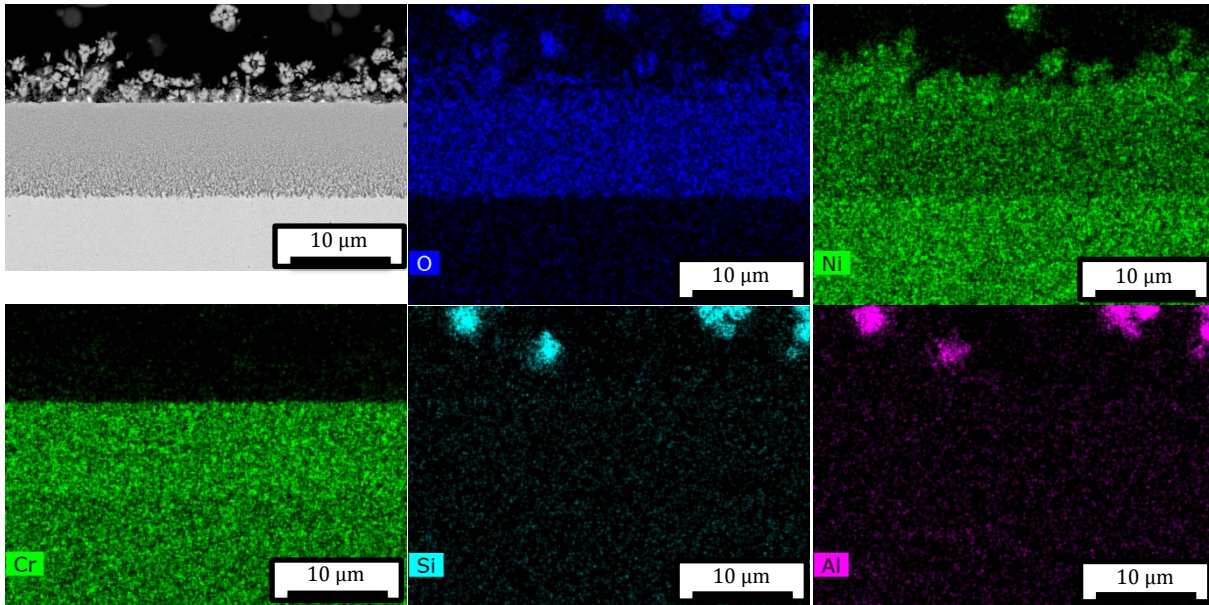
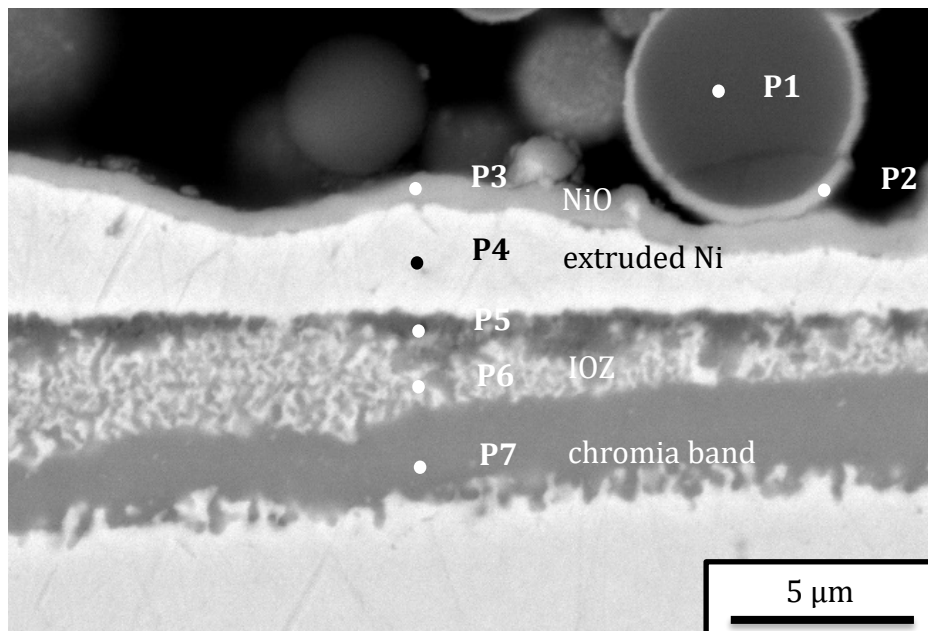


Figure. 3 – BSE-SEM cross-section and EDS mapping of Ni-25Cr after 300 h reaction beneath 100% ash deposit in Ar-60CO₂-20H₂O at 650°C.

EDS-point analysis was carried out on the dominant structure formed in the 10% salt case (Fig. 4). The results confirmed that the outer thin oxide is NiO (P3 in Fig. 4), with extruded Ni metal (P4 in Fig. 4) below it. A Cr-rich IOZ was formed (P6 in Fig. 4), with a rather thick chromia band (P7 in Fig. 4) at the reaction front. Locally Cr-rich inner oxides were found beneath the Ni metal-IOZ interface (P5 in Fig. 4). Moreover, both Na and K were detected within the ash particle (P1 in Fig. 4), and a layer of NiO was observed to have enveloped an ash particle (P2 in Fig. 4).



Point (at %)	Ni	Cr	O	Na	K	Ca	Fe	Al	Si
1	4.1	-	55.3	1.5	1.9	2.0	0.5	12.3	22.4
2	28.5	3.3	46.9	1.5	-	-	1.0	6.6	12.1
3	43.3	4.9	41.5	-	-	-	-	2.9	7.3
4	98.5	1.5	-	-	-	-	-	-	-
5	22.5	39.2	38.3	-	-	-	-	-	-
6	38.9	29.6	31.4	-	-	-	-	-	-
7	2.3	45.6	52.1	-	-	-	-	-	-

Figure. 4 – BSE-SEM cross-section of Ni-25Cr after 300 h reaction beneath 90% ash + 10% salt deposit in Ar-60CO₂-20H₂O at 650°C (dominant structure).

A localized attack appeared on the alloy under the 90% ash + 10% chloride deposit is shown in Fig. 5. A relatively thick Cr₂O₃ (~4.5 μm) scale had formed and contained some encapsulated metallic nickel. Subsurface voids are seen to penetrate up to 17 μm into the alloy at this scale. EDS-mapping analysis (Fig. 5) confirmed the existence of the outer Cr₂O₃ layer. Moreover, it should be noted that Na and K enrichment correspond well with the location of ash particles.

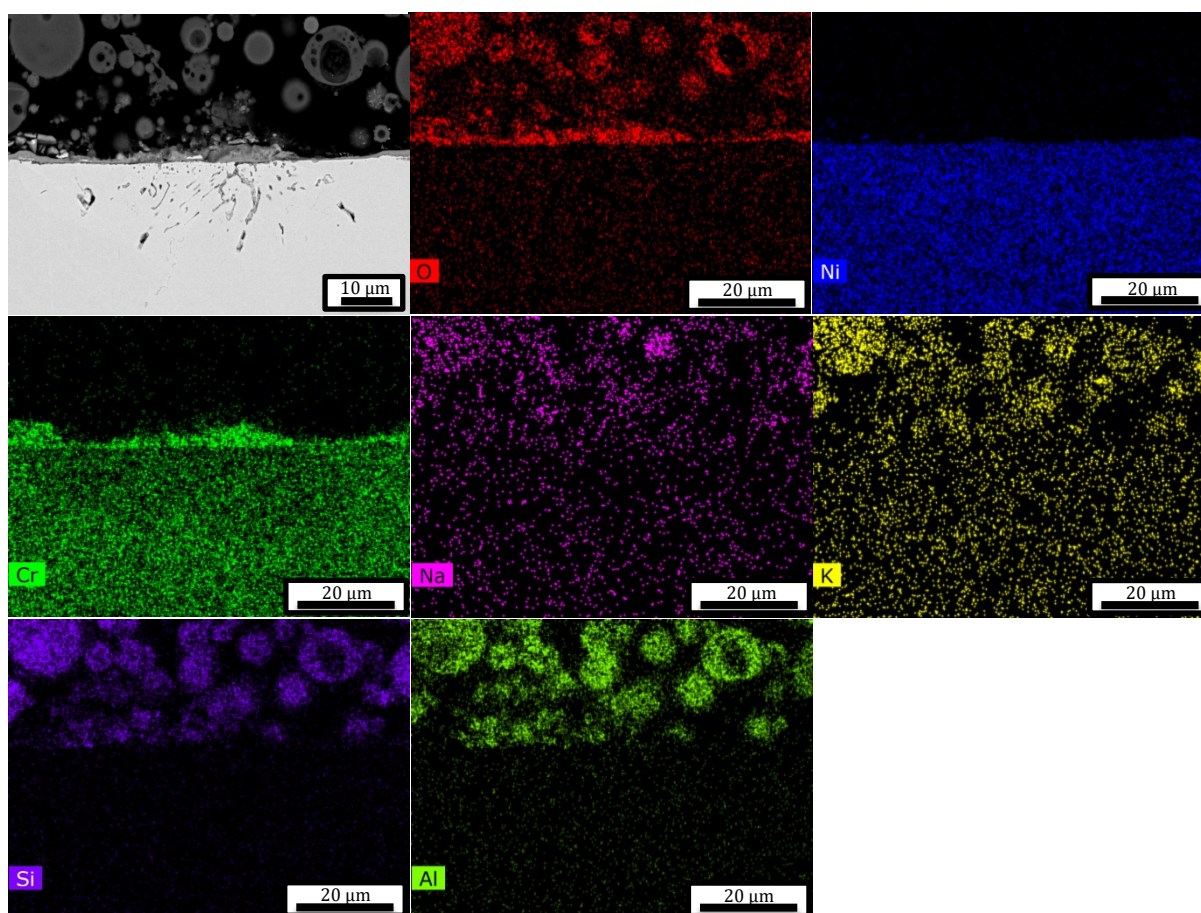


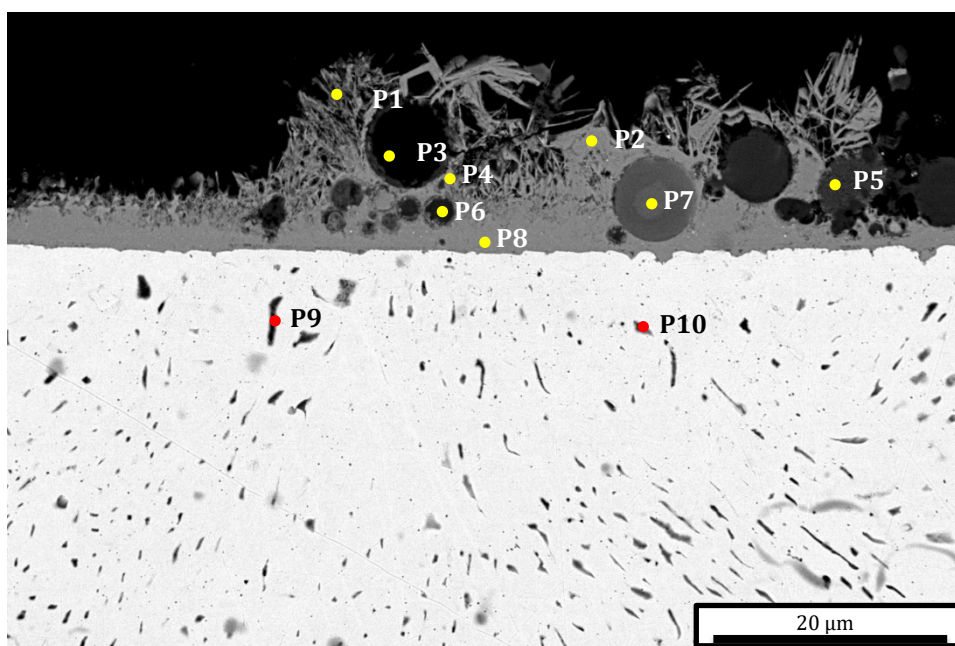
Figure. 5 – BSE-SEM cross-section and EDS mapping of Ni-25Cr after 300 h reaction beneath 90% ash + 10% salt deposit in Ar-60CO₂-20H₂O at 650°C (localised structure).

Further increasing the salt content to 50%, a thick oxide layer and subsurface internal precipitate structure became dominant, and the enlarged view of them is shown in Fig. 6. Very porous Cr_2O_3 formed externally (P2, P4, and P8 in Fig. 6), where several ash particles (P3, P5, P6, and P7 in Fig. 6) were encapsulated by the thick chromia layer. The outermost part of chromia layer was in a feathery shape (P1 in Fig. 6). Internal precipitates were found to be a mixture of Cr-rich oxides (P9 in Fig. 6) plus some subsurface voids.

SEM-EDS analyses were also carried out on the localized structure formed in the 50% salt case (Fig. 7). A thin protective layer was composed of an external Ni-rich oxide layer (P1 in Fig. 7, the Cr signal could be attributed to the surrounding area) and an inner Cr-rich oxide layer (P2 in Fig. 7).

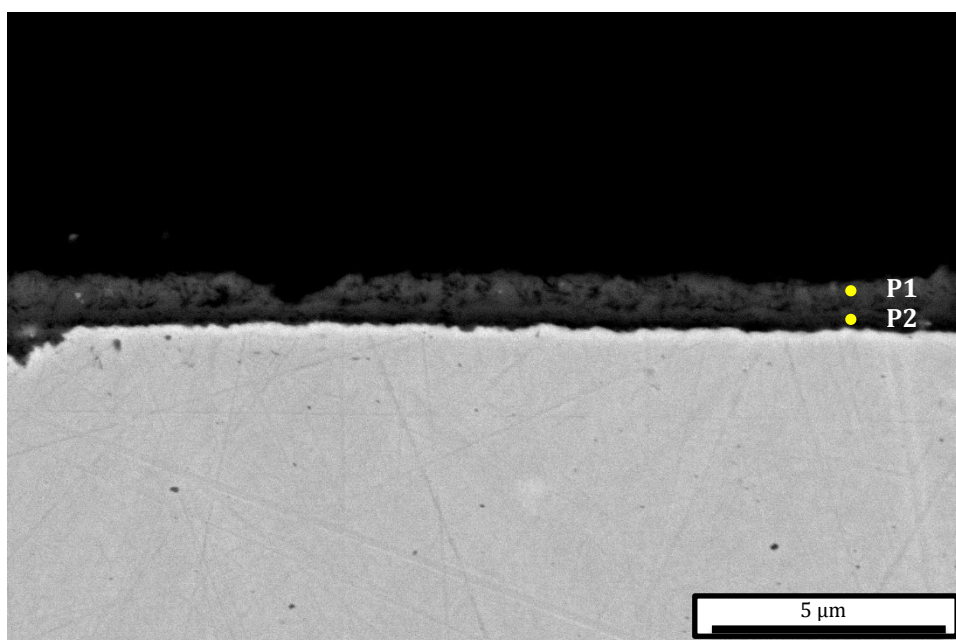
After coating with the 75% salt deposit (Fig. 8), the external Cr_2O_3 layer (P3, P4, and P5 in Fig. 8) was even thicker, and a more compact Cr_2O_3 band (P7 in Fig. 8) was found below the thick external layer, with an extruded metallic layer (P6 in Fig. 8) between them. Cr depletion (P8 in Fig. 8) was detected in the precipitates (P9, P10, and P11 in Fig. 8) region. A considerable amount of Na (13.1 at.%, P9 in Fig. 8) was detected in one of the oxides formed in the subsurface area.

Fig. 9 shows an enlarged SEM image of the 100% salt case. Two different reaction morphologies were observed, with the structure marked by a white rectangle occupying about 60% of the alloy surface. Enlargement of this structure in Fig. 9 revealed that the outermost light contrast area is NiO (P2 in Fig. 9), which contained some pores, and inside those pores, Na could be detected (P7 in Fig. 9). A darker band in the middle was Cr-rich (P3 in Fig. 9), as were the oxide precipitates in the underlying IOZ (P4, P5, and P6 where the Cr content is increased in the innermost region). The second structure seen in Fig. 9 (dark contrast region marked P1), was a thick Cr_2O_3 layer with pores beneath it.



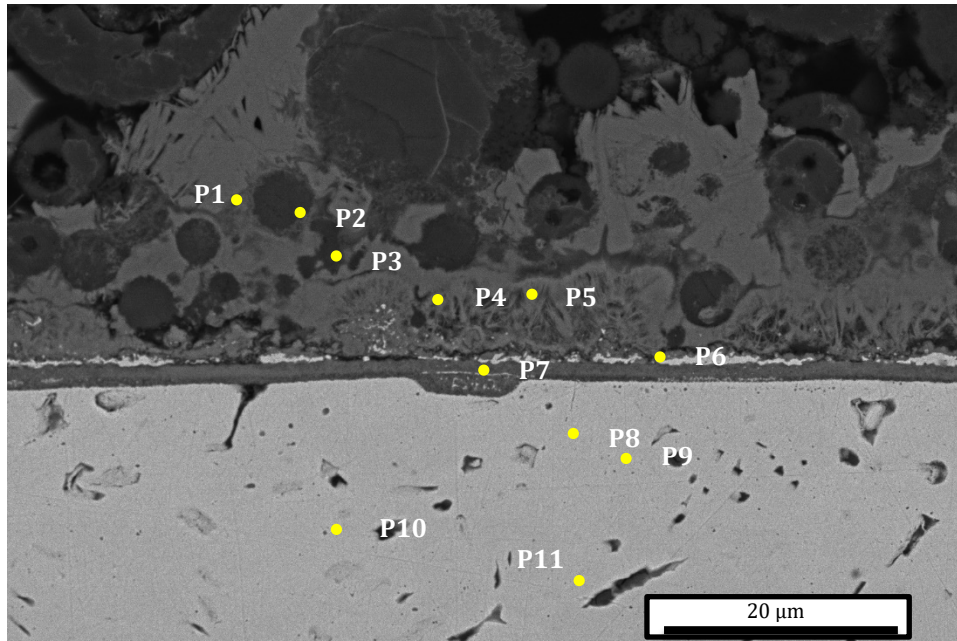
Point (at %)	Ni	Cr	O	Na	K	Cl	Si	Al	Mg	Fe	Ca	Ti
1	1.9	46.6	49.2	1.0	0.7	-	-	-	-	-	0.5	-
2	0.8	41.2	51.4	-	-	-	4.0	2.5	-	-	-	-
3	-	16.7	64.6	6.7	7.2	4.7	-	-	-	-	-	-
4	-	56.0	44.0	-	-	-	-	-	-	-	-	-
5	-	0.8	52.5	5.9	4.3	-	17.6	11.0	-	-	1.8	6.2
6	-	47.5	52.5	-	-	-	-	-	-	-	-	-
7	-	8.5	52.0	-	1.3	-	16.4	10.8	1.7	9.4	-	-
8	-	48.4	51.6	-	-	-	-	-	-	-	-	-
9	35.4	35.0	25.3	-	-	4.3	-	-	-	-	-	-
10	32.3	67.7	-	-	-	-	-	-	-	-	-	-

Figure. 6 – BSE-SEM cross-section of Ni-25Cr after 300 h reaction beneath 50% ash + 50% salt deposit in Ar-60CO₂-20H₂O at 650°C (dominant structure).



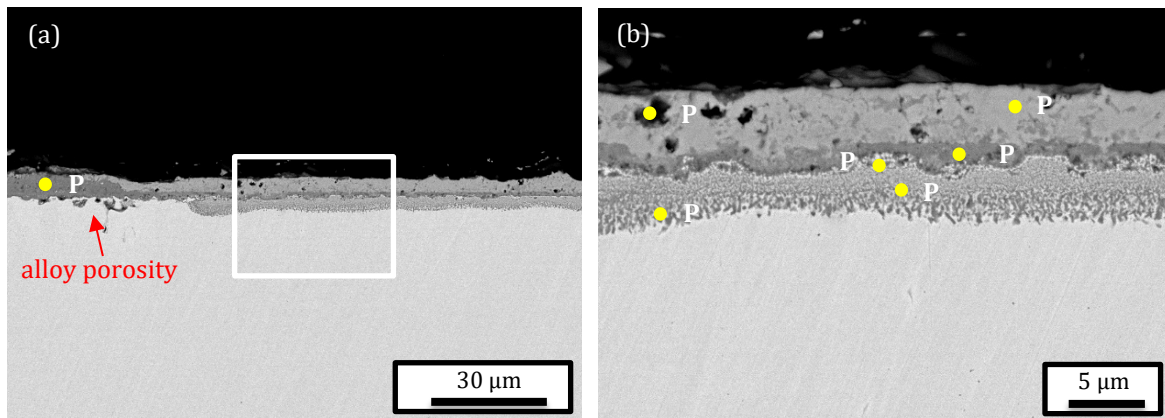
Point (at %)	Ni	Cr	O	Si	Ca
1	20.8	24.9	50.9	2.2	1.2
2	9.0	40.8	49.1	1.1	-

Figure. 7 – BSE-SEM cross-section of Ni-25Cr after 300 h reaction beneath 50% ash + 50% salt deposit in Ar-60CO₂-20H₂O at 650°C (localised structure).



Point (at %)	Ni	Cr	O	Na	Cl	Si	Al	Ca
1	-	7.9	61.4	0.9	0.9	13.9	14.6	0.4
2	-	25.0	60.9	0.8	1.5	8.0	3.8	-
3	-	36.1	59.5	-	1.6	2.8	-	-
4	1.9	35.8	59.2	2.5	-	0.6	-	-
5	0.7	37.8	60.0	0.8	-	0.7	-	-
6	81.3	5.3	13.1	0.3	-	-	-	-
7	1.9	38.9	58.4	0.8	-	-	-	-
8	81.9	18.1	-	-	-	-	-	-
9	46.3	12.9	27.7	13.1	-	-	-	-
10	85.5	9.4	5.1	-	-	-	-	-
11	45.5	9.9	38.3	4.4	1.9	-	-	-

Figure. 8 – BSE-SEM cross-section of Ni-25Cr after 300 h reaction beneath 25% ash + 75% salt deposit in Ar-60CO₂-20H₂O at 650°C.



Point (at %)	1	2	3	4	5	6	7
Ni	0.8	54.1	7.7	58.5	43.8	22.3	44.9
Cr	43.1	1.6	40.1	17.0	26.8	35.4	11.5
O	56.1	44.3	52.2	24.5	29.4	42.4	29.3
Na	-	-	-	-	-	-	14.3

Figure. 9 – (a) BSE-SEM cross-section of salt deposited Ni-25Cr after 300 h reaction in Ar-60CO₂-20H₂O at 650°C, and (b) enlarged view of the rectangular area in (a).

In order to further reveal the subsurface precipitates (mainly pore structure) formed in the salt containing case, a series of FIB sectioning analyses have been carried out (Fig. 10). The reconstructed imaging of the alloy (Fig. 10(a)) shows that the pores are densely distributed in the upper area, and the density decreases with increasing depth, this is also confirmed by the depth profile as shown in Fig. 10(b). According to the 2D EBSD results (Fig. 10(c)), the pores are likely to be located on the grain boundaries instead of inside the grains.

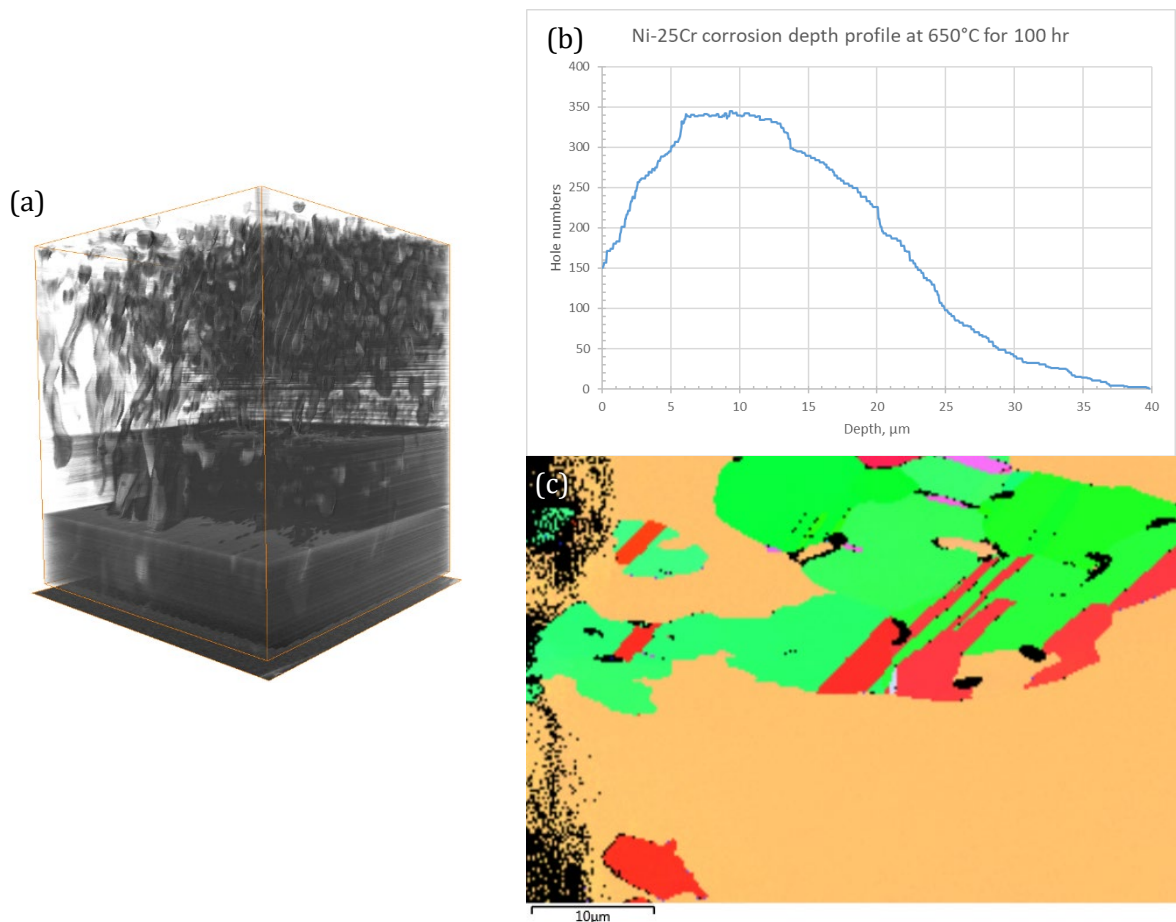


Figure. 10 – (a) PFIB 3-D reconstruction, (b) corrosion depth profile, and (c) 2D EBSD IPF map of Ni-25Cr after 100 h reaction 100% salt deposit in Ar-60CO₂-20H₂O at 650°C.

DISCUSSION

The above results showed that in the gas-only condition, Ni-25Cr formed a more or less uniform oxide scale, consisting of an internal oxidation zone covered by a Ni layer with a thin NiO layer on the top surface (Fig. 1). Adding salts and/or ash deposits on the surface changed oxide structure and morphology and produced non-uniform oxide scales as summarised in Table 3.

Table 3. Summarised oxide products (thicknesses and occupying proportions) formed on Ni-25Cr under varied conditions

	650 °C			
	Protective/partial protective region		Deep internal attack region	
	µm	%	µm	%
Gas-only	6	100	0	0
100% ash	9	100	0	0
90% ash + 10% salt	5	90	23	10
50% ash + 50% salt	7	20	43	80
25% ash + 75% salt	0	0	120	100
100% salt	8	70	46	30

* For the internal attack region, only the depths of the internal attacks were measured.

The presence of chloride salts altered reaction morphologies significantly. There were two major oxide structures formed: partial protective region and deep internal attacked region with numerous internal precipitates/voids. After 90 wt.% coal ash was added to the salts, a predominant structure with pure Ni layer (Figs. 6, 9(a)) appeared, similar to that seen in the gas-only condition (Fig. 1), where 10% of the alloy surface was covered by the thick Cr₂O₃ layer with deep internal voids beneath. By increasing the salt content to 50%, the thick oxide layer and subsurface internal precipitate structure became dominant, with localised thinner protective layer forming. For the 25 wt.% ash + 75 wt.% salt, the whole alloy surface was covered by the thick oxide layer with deep internal penetration.

The discussion will first examine the chloride effects on oxide formation and morphology, and then the synergistic effect of chloride salts and ash will be considered.

4.1 Effect of chlorides on oxide formation and morphology

The alloy that had no deposit formed a uniform internal oxidation zone (IOZ) containing Cr-rich oxide and an external Ni layer with large, dispersed Ni nodules surmounted by a thin NiO scale. This oxide product morphology was typically observed in water vapour containing atmosphere with low-oxygen partial pressure [11]: metallic Ni was ejected from the IOZ to allow the growth of chromia precipitates, and the metallic Ni was slowly oxidised due to the retarding effect of H₂O.

The presence of chloride salt significantly altered the constituents and morphology of the oxide products: a relatively thick, multi-layered oxide scale covered the majority of the alloy surface, and a thick chromium-rich oxide developed in the remaining areas. The localised Cr₂O₃ layer was thick and relatively porous, containing some Ni particles with densely distributed subsurface voids (Fig. 9(a)).

The different oxide morphologies were due to the so-called “Cl-induced active oxidation”. Cl₂ formed by the reaction between chloride salts and water vapour from the atmosphere, which provides the condition for active corrosion to initiate [6, 12, 13]. Metal or metal oxides could react with the Cl₂ to form metal chlorides inside the oxide scale and/or in the internal region. When the volatile chlorides reach the oxide-gas interface, where the p_{O_2} is higher, they can be reconverted back to oxides, but with very porous nature. The liberated Cl₂ can subsequently participate in the active reaction again, forming loose, porous oxides, and even developing pores inside the alloys:



Here, the forward Eq. 2 depicts oxide volatilisation, which is favoured where p_{Cl_2} is higher. The reverse reaction, on the other hand, describes chloride re-oxidation and deposition externally where p_{O_2} is higher.

The possibility of Ni, Cr and their oxides reacting with chlorine has been evaluated in the same reaction condition [14]. It has been concluded that the volatilisation of Ni and NiO is unlikely, while Cr and Cr₂O₃ could form highly volatile chlorides when p_{O_2} at the equilibrium Cr/Cr₂O₃ is used. When the volatile chloride reaches the alloy surface where p_{O_2} is high, it can be converted back to its oxide, and the thick, porous Cr₂O₃ layer is formed. In this case, the thick chromia layer is non-protective due to its porous nature.

The way in which arrayed pores develop in the subsurface alloy region (Figs. 9(b), 10(a)) is of interest. PFIB 3-D reconstruction was performed to reveal the interconnected pore channels. It has been found that intragranular carbides were formed within Ni-25Cr [14] exposed to the same gas. Both Cr₂₃C₆ or Cr₇C₃ are thermodynamically favoured to react with Cl₂, producing CO and the volatilised CrCl₂, producing the observed voids. This is also confirmed by the 2D EBSD results where most of the pores lay along the grain boundaries.

4.2 Effect of ash particles on Ni-25Cr corrosion

After 100% ash deposit was coated on the alloy surface, the oxide formed was very similar to that formed in the gas-only case (Fig. 2). The differences between those two cases are: the thickness of the IOZ increased from 5 μm to 10 μm, the oxide volume fractions of IOZ increased from 0.79 ± 0.01 (gas-only case) to 0.87 ± 0.01 (ash-only case); the extruded Ni layer became discontinuous in the 100% ash case; and more part of the metallic Ni nodules on the top were converted to NiO. Those difference are mainly caused by the obstacle effect of ash particles which alleviate the effect of water vapour.

The first typical reaction products for Ni-25Cr under a deposit of ash and chloride are NiO + extruded Ni + IOZ with or without a chromia band; structure with thick Cr₂O₃ layer with underneath arrayed voids and precipitate occurred with the presence of chloride salts. With the increasing content of chloride salt, the deep internal attack region fraction increased as well (Table 3). It should be noted that the amount of chlorides (3.0 ± 0.5 mg/cm²) is comparable to that under the salt only condition (2.5 ± 0.5 mg/cm²), these oxide scale constitutions were not the same as those in the salt-only condition. Noting from Table 3 that the extent of reaction is essentially the same in the gas-only and the two gas + ash + salt conditions, it is concluded that salt effects are largely in operative when the deposit contains mainly ash.

Solid ash particles were generally considered innocuous in the degradation of high temperature alloys because of their comparatively stable structure and chemistry (mainly silica and alumina). Additionally, the recurrence of the extruded Ni metal proves that the water vapor's ability to slow NiO development, as seen in the gas-only example, is still in effect. The lack of a salt influence on reaction morphology can be explained most simply by the fact that not enough salt makes contact with the surface to produce the salt effect. Additionally, because of how loosely the ash particles are packed, gas, including water vapor, can get to the scale's surface. This allows for the maintenance of the nickel oxidation-retarding effect of water vapour.

When Ni-25Cr was deposited with ash + chloride, the 'wetting' of ash particles by NiO was observed on top of the outer scale (P2 in Fig. 4). This is thought to be the result of rapid NiO nucleation and growth on the ash particle surface.

CONCLUSIONS

A model Ni-25Cr (wt.%) alloy coated with chlorides, coal ash and the mixtures of them (salt/ash weight ratios 10/90, 50/50, 75/25) was exposed in Ar-60CO₂-20H₂O at 650 °C for 300 h. For comparison, the alloy without any deposit was also exposed to the same gas.

In the gas-only condition, Ni-25Cr alloy formed a uniform IOZ and an external nickel layer together with some nickel nodules surmounted by a thin NiO scale. The formation of this metallic nickel was attributed to the volume expansion of the IOZ because of Cr-rich oxide precipitation.

Salt deposits changed the scale structure and morphology, and produced a non-uniform oxide scale. Predominantly, a duplex scale of NiO over a thin Cr₂O₃ layer with an underlying IOZ was found in salt-coated samples after reaction. In the case of chloride salt, an active oxidation mechanism accounts for outward Cr transport and porous chromia layer formation. In the presence of chlorides, local regions of the Cr₂O₃ scale contained encapsulated Ni metal with underlying subsurface alloy porosity. The disappearance of nickel layer in the case of salt-coated samples indicated that Cl each interacted with NiO surface and grain boundaries, interfering with the retarding effect of water otherwise observed for nickel oxidation.

Under a deposit of 100% ash, the oxide product structure is generally the same with the gas-only case, the main difference is the disappearance of the extruded metallic Nickel, this is due to the presence of ash which reduces the effect of water vapour.

Under a deposit of ash and chloride salt mixture, two different oxide structure formed, one is mainly similar to the one formed in the gas-only case, the other is composed of thick Cr₂O₃ and deep internal penetration. The fraction of the deep penetration structure increases with the increasing amount of chloride salt. This phenomenon is attributed to dilution by ash and greatly reduced salt-scale contact.

ACKNOWLEDGMENTS

Financial support from the Australian Research Council's Discovery Program is gratefully acknowledged.

References

1. Stanger, R., Wall, T., Spörl, R., Paneru, M., Grathwohl, S., Weidmann, M., Scheffknecht, G., McDonald, D., Myöhänen, K., and Ritvanen, J.J.I.j.o.g.g.c., *Oxyfuel combustion for CO₂ capture in power plants*. 2015. **40**: p. 55-125.
2. Yin, C. and Yan, J., *Oxy-fuel combustion of pulverized fuels: Combustion fundamentals and modeling*. Applied Energy, 2016. **162**: p. 742-762.
3. Zeng, Z., Natesan, K., Cai, Z., and Rink, D., *Effect of coal ash on the performance of alloys in simulated oxy-fuel environments*. Fuel, 2014. **117**: p. 133-145.
4. Yin, C. and Yan, J.J.A.E., *Oxy-fuel combustion of pulverized fuels: Combustion fundamentals and modeling*. 2016. **162**: p. 742-762.
5. McNallan, M., Liang, W., Oh, J., and Kang, C., *Morphology of corrosion products formed on cobalt and nickel in argon-oxygen-chlorine mixtures at 1000 K*. Oxidation of Metals, 1982. **17**(5): p. 371-389.
6. Grabke, H., Reese, E., and Spiegel, M., *The effects of chlorides, hydrogen chloride, and sulfur dioxide in the oxidation of steels below deposits*. Corrosion Science, 1995. **37**(7): p. 1023-1043.
7. Brown, M., DeLong, W., and Auld, J., *Corrosion by chlorine and by hydrogen chloride at high temperatures*. Industrial Engineering Chemistry, 1947. **39**(7): p. 839-844.
8. Koutsoyiannis, D., *Clausius–Clapeyron equation and saturation vapour pressure: simple theory reconciled with practice*. European Journal of physics, 2012. **33**(2): p. 295.
9. *FactSage 8.1 Thermochemical Software and Database (accessed July 2022)*. 2022.
10. Cai, Y., Nguyen, T.D., Zhang, J., Gleeson, B., and Young, D.J., *Corrosion behaviour of Fe-25Cr alloy in wet CO₂ gas at 650° C: Effects of chloride deposits and Si+ Mn alloying addition*. Corrosion Science, 2022. **195**: p. 110001.
11. Xie, Y., Zhang, J., and Young, D.J., *Water vapour effects on corrosion of Ni-Cr alloys in CO₂ gas at 650° C*. Corrosion Science, 2018. **136**: p. 311-325.
12. Ihara, Y., Ohgame, H., Sakiyama, K., and Hashimoto, K., *The corrosion behaviour of chromium in hydrogen chloride gas and gas mixtures of hydrogen chloride and oxygen at high temperatures*. Corrosion Science, 1983. **23**(2): p. 167-181.
13. Ihara, Y., Ohgame, H., Sakiyama, K., and Hashimoto, K., *The corrosion behaviour of iron in hydrogen chloride gas and gas mixtures of hydrogen chloride and oxygen at high temperatures*. Corrosion Science, 1981. **21**(12): p. 805-817.
14. Cai, Y., Nguyen, T.D., Zhang, J., Gleeson, B., and Young, D.J., *Corrosion Behaviour of Fe-based Austenitic Alloys and Ni-based Alloys in Wet CO₂ Gas with and without Chloride Deposits at 650°C (as submitted)*.

AUTHOR DETAILS



A. CAI is the first author of this paper. She is PhD student at UNSW. She is responsible for the conceptualization, methodology, data curation, writing-original draft preparation.



B. Zhang is the corresponding author of this paper. He is Professor at the School of Materials Science and Engineering, UNSW. His role in this paper is supervision, writing-reviewing and editing.



C. Young is the Emeritus Professor at UNSW, a position he has held since 2003. He is responsible for the supervision, writing-reviewing and editing.